Contents lists available at ScienceDirect

Scripta Materialia

journal homepage: www.journals.elsevier.com/scripta-materialia



Computational thermodynamics-guided alloy design and phase stability in CoCrFeMnNi-based medium-and high-entropy alloys: An experimental-theoretical study

David D.S. Silva ^{a,b,*}, Gustavo Bertoli ^{a,b}, Nelson D. Campos Neto ^b, Norbert Schell ^c, Kester D. Clarke ^{b,d}, Michael J. Kaufman ^b, Amy J. Clarke ^{b,d}, Francisco G. Coury ^e, Claudemiro Bolfarini ^e

- ^a Federal University of São Carlos, Graduate Program in Materials Science and Engineering, 13565-905, São Carlos, SP, Brazil
- b Colorado School of Mines, George S. Ansell Department of Metallurgical and Materials Engineering, 80401, Golden, CO, USA
- ^c Helmholtz-Zentrum Hereon, Institute of Materials Physics, Max-Planck-Str. 1, 21502, Geesthacht, Germany
- d Los Alamos National Laboratory, Sigma Manufacturing Science Division, 87545, Los Alamos, NM, USA
- ^e Federal University of São Carlos, Department of Materials Engineering, 13565-905, São Carlos, SP, Brazil

ARTICLE INFO

Keywords: Medium- and high-entropy alloys CALPHAD Thermodynamic calculations Sigma phase High-energy synchrotron X-ray diffraction

ABSTRACT

A computational thermodynamics approach has been employed to design CoCrFeMnNi-based medium- and high-entropy alloys (M/HEAs) with systematically varied compositions (Co(($_{80-X}$)/ $_2$)Cr(($_{80-X}$)/ $_2$)Fe_XMn₁₀Ni₁₀ with x=30, 40, and 50 at.%) and phase stability. Since the formation of sigma phase, usually brittle and undesirable, is a common concern, when this class of alloys is subjected to elevated temperatures (600–1000 °C), predicting its formation becomes essential. Thus, its formation and the phase equilibria were studied using the CALPHAD method, and two empirical methods, namely, valence electron concentration (VEC) and paired sigma-forming element (PSFE). Isothermal aging treatments at 900–1100 °C for 20 h were performed, since CALPHAD and VEC/PSFE predictions diverged. Both prediction methods were compared with experimental characterization by a combination of scanning electron microscopy and high-energy synchrotron X-ray diffraction. The predictions from the VEC/PSFE and CALPHAD calculations (depending on the database used) were shown to be quite accurate.

Medium/high entropy alloys (M/HEAs) are attracting considerable attention in the literature due to the good combination of properties exhibited by some compositions, such as excellent mechanical response, and excellent oxidation and corrosion resistance [1,2]. While initially equiatomic M/HEAs were mostly produced [3,4], Recently the focus shifted to compositions with optimized properties, which typically happens at non-equiatomic compositions [5–7]. Therefore, accurate ways of determining temperature-dependent phase stabilities for large composition fields are of great interest [8].

The most used computational methods for M/HEAs design include the calculation of phase diagrams (CALPHAD), density functional theory, molecular dynamics, and Monte Carlo [9]. Of these, CALPHAD-type approaches, in general have broader applicability and have been shown to be useful in predicting phase stability in several cases [10,11]. However, for cases in which competing intermetallic phases appear,

such as Laves (C14, C15, C36, and PuNi₃), A15, chi (χ), mu (μ), and sigma (σ), this approach currently has limited predictive power [12–15].

Regarding the sigma phase, its formation is a real concern for face-centered cubic (FCC) alloys subjected to elevated temperatures (600–1000 °C); and, it is frequently observed in the CoCrFeMnNi system [16,17]. Its precipitation can be responsible for embrittlement, and loss of corrosion and oxidation resistance [18–22]. Therefore, predicting its formation is essential. Considering that predicting sigma phase formation using CALPHAD can be unreliable on novel compositions [23], Tsai et al. [24,25] formulated two criteria to predict the formation of the sigma phase: valence electron concentration (VEC) and paired sigma-forming element (PSFE), here called the "Tsai criteria". In summary, the Tsai criteria predict the alloys will be: i) sigma-free, if the VEC is outside the range of 6.8 and 7.84 *or* the PSFE is lower than 25 %; ii) sigma-prone, if the VEC is inside the range of 6.88 and 7.84 *and* the PSFE

E-mail address: david.domingos20@gmail.com (D.D.S. Silva).

^{*} Corresponding author.

is higher than 40 %; iii) uncertain about sigma phase formation, if the VEC is inside the range of 6.88 and 7.84 *and* the PSFE is inside the range of 25 % and 40 %.

In this study, we critically evaluate both the CALPHAD and Tsai criteria prediction methods, comparing their accuracies and identifying the factors influencing their precision. Additionally, we compare these prediction methods with experimental characterization, employing scanning electron microscopy and high-energy synchrotron X-ray diffraction to validate our predictions. Although comparisons and validations between the methods used (CALPHAD and Tsai criteria) will be performed, the main focus of this work is to design new M/HEAs derived from the Cantor alloy with enhanced FCC phase stability, thereby making the formation of single-phase compositions more likely. This work significantly contributes to our understanding of the CoCrFeMnNi system, particularly regarding its potential susceptibility to sigma phase formation. Our findings have the potential to provide valuable guidance for future alloy design and optimization efforts.

The M/HEAs in the $Co_{((80-X)/2)}Cr_{((80-X)/2)}Fe_XMn_{10}Ni_{10}$ system, with x=30, 40 and 50, at.%, were designed and resulted in the following nominal compositions: $Co_{15}Cr_{15}Fe_{50}Mn_{10}Ni_{10}$, $Co_{20}Cr_{20}Fe_{40}Mn_{10}Ni_{10}$, and Co₂₅Cr₂₅Fe₃₀Mn₁₀Ni₁₀ (at.%), hereinafter denoted by Co15Cr15, Co20Cr20 and Co25Cr25, respectively. Thermodynamic calculations were performed to estimate the equilibrium phases at different temperatures. These calculations were performed using two recent thermodynamic databases for M/HEAs, TCHEA5 (Thermo-Calc® software (version 2021b)) and PanHEA2022 (Pandat® software (version 2022)). For the CoCrFeMnNi system, the TCHEA5 database describes 10/10 binary (fraction of assessed binaries $f_{AB} = 1$) and 5/10 ternary systems (fraction of assessed ternaries $f_{AT} = 0.5$). In contrast, the PanHEA2022 database fully describes 10/10 binaries ($f_{AB} = 1$) and 8/10 ternaries (f_{AT} = 0.8). Specifically, Miracle and Senkov [1] suggested that for a database to be suitable, it is important that $f_{AB} = 1$ and that one has the highest possible value of f_{AT} . However, the prediction reliability also depends on the thermodynamic model adopted to describe the constituent phases [26,27]. The sigma phase has a tetragonal lattice (space group #136 P42/mnm, Pearson symbol tP30) containing 30 atoms per unit cell, which are divided into five Wyckoff positions (2a, 4f, 8i, 8i', and 8j) [26]. PanHEA2022 database uses the three sublattices model (8i')₈ (4f)₄ (2a,8i,8j)₁₈ or (Co,Cr,Fe,Mn,Ni)₈ (Cr,Fe)₄ (Co,Cr,Fe,Mn,Ni)₁₈ to describe the sigma phase, where not all constituent elements can occupy any sublattice. In contrast, TCHEA5 database uses another three sublattices model: (2a,8i')₁₀ (4f)₄ (8i,8j)₁₆ or (Co,Cr,Fe,Mn,Ni)₁₀ (Co,Cr, Fe,Mn,Ni)₄ (Co,Cr,Fe,Mn,Ni)₁₆. Thus, although the PanHEA2022 database has a higher fraction of assessed ternaries for this system, TCHEA5 provides a more comprehensive description of the sigma phase. Therefore, a comparative analysis will be performed here.

Two empirical methods (Tsai criteria) were also used to predict the formation or absence of the sigma phase. The 1st Tsai criterion [24] is based upon the VEC of the alloy, which is a weighted average (by atomic fraction) of the VEC of the constituent components [1,24] and may be calculated according to Eq. (1) [24]:

$$VEC = \sum_{i=1}^{n} c_i (VEC)_i \tag{1}$$

where n is the number of components in the alloy, and c_i is the atomic fraction of the i^{th} component. According to the 1st Tsai criterion, the sigma phase is not formed in alloys with VEC values outside the range between 6.88 and 7.84. However, some binary alloys, even those where the VEC predicts sigma phase formation, do not have sigma in their phase diagram, e.g., the Fe-Mn system, where the FeMn composition has a VEC of 7.5 [28]. For this reason, Tsai et al. [25] proposed a 2nd criterion that introduced the new parameter, PSFE.

The PSFE considers if the constituent elements are sigma-prone when in solid solution, and will be given by:

$$PSFE(c_A, c_B) = \begin{cases} 2\sum c_A, & \text{if } \frac{\sum c_A}{\sum c_B} \le 1\\ 2\sum c_B, & \text{otherwise} \end{cases}$$
 (2)

where c_A and c_B are the atom fractions of A and B, respectively. According to the 2nd Tsai criterion, the sigma phase should not form in alloys with PSFE $\langle 25 \%$ and should form in alloys with PSFE \rangle 40 %. Between these limits, the sigma phase may or may not form.

In the current work, the A elements (transition metals of groups VB-VIIB) could be Cr and Mn, whereas B elements (transition metals of groups VIIB-VIIIB) could be Mn, Fe, Co, and Ni. To properly select elements A and B, and to obtain greater accuracy in the predictions, all binary phase diagrams [28] of the CoCrFeMnNi system were consulted to identify those that exhibit the sigma phase at three different temperatures, 900, 1000, and 1100 $^{\circ}$ C. Table S1 (supplementary materials section) compiles the sigma-prone binaries for the temperatures evaluated. Based on Table S1, Cr is an A element; Mn, Fe, and Co are B elements; and Ni is neither an A nor a B element.

The ingots were produced by vacuum induction melting. All raw materials used for casting the alloys were commercially available pure elements. 0.5 at.% Al was added as a deoxidizer to avoid large angular oxide inclusions. After solidification, the as-cast ingots were homogenized at 1200 °C for 2 h, followed by water quenching. The homogenized alloys were hot rolled at 1100 °C with a total rolling reduction ratio of \approx 87.5 %, followed by water quenching. After hot rolling, the alloys were cold-rolled with a total reduction ratio of ≈ 50 %. Samples with dimensions 10×10×1 mm³ were produced by wire electrical discharge machining (EDM) from the alloy sheets. The first group of samples were then annealed at 900 °C for 0.25 h, followed by water quenching to obtain fully recrystallized microstructures, whereas the second group of samples were aged at 900, 1000, and 1100 °C for 20 h, followed by water-quenching to allow the formation of the sigma phase. According to the results reported in the literature [16,17], it is reasonable to suppose that an aging time of 20 h provides sufficient time for the sigma phase to form. Furthermore, plastic deformation during cold rolling can also accelerate its formation by providing heterogeneous nucleation sites and high defect density [29].

Chemical analysis of the major alloying elements (Co, Cr, Fe, Mn, Ni and Al) was carried out using inductively coupled plasma-optical emission spectrometry (ICP-OES, Thermo 6000). The interstitial elements (C, S, O, N, and H) were also determined - C and S by direct combustion in a Leco® CS-844 analyzer, O and H by infrared absorption radiation, and N by thermal conductivity in a Leco® ONH-836 analyzer. The microstructures of the M/HEAs were investigated using a TESCAN S8252G scanning electron microscope (SEM) equipped with an energy dispersive spectroscopy (EDS) and a backscattered electron (BSE) detectors. A FEI Helios Nanolab 600i was used for electron backscatter diffraction (EBSD) analysis.

High-energy synchrotron X-ray diffraction (HE-SXRD) was used to identify the phase structure evolution. The synchrotron experiments were performed at the P07B High Energy Materials Science beamline of PETRA III/DESY [30]. A high-photon beam energy of 87.1 KeV was used. This photon energy allowed performing diffraction experiments in transmission mode. LaB₆ powder was used as a standard for the calibration of the instrument parameters, and to determine the sample-to-detector distance. A two-dimensional PerkinElmer fast detector was used to collect the Debbye-Scherrer rings.

Phase predictions under equilibrium are plotted in Fig. 1 (a-f) using TCHEA5 database (Fig. 1 (a-c)) and PanHEA2022 database (Fig. 1 (d-f)). For both databases, the three alloys are predicted to be single-phase FCC at 1200 °C. Sigma phase is predicted to form from the FCC phase after solidification is complete, but not until temperatures below 1180 °C (Fig. 1(c)) and 912 °C (Fig. 1(f)) were attained, depending on the alloy and database, with increasing volume fractions at lower temperatures

D.D.S. Silva et al. Scripta Materialia 252 (2024) 116264

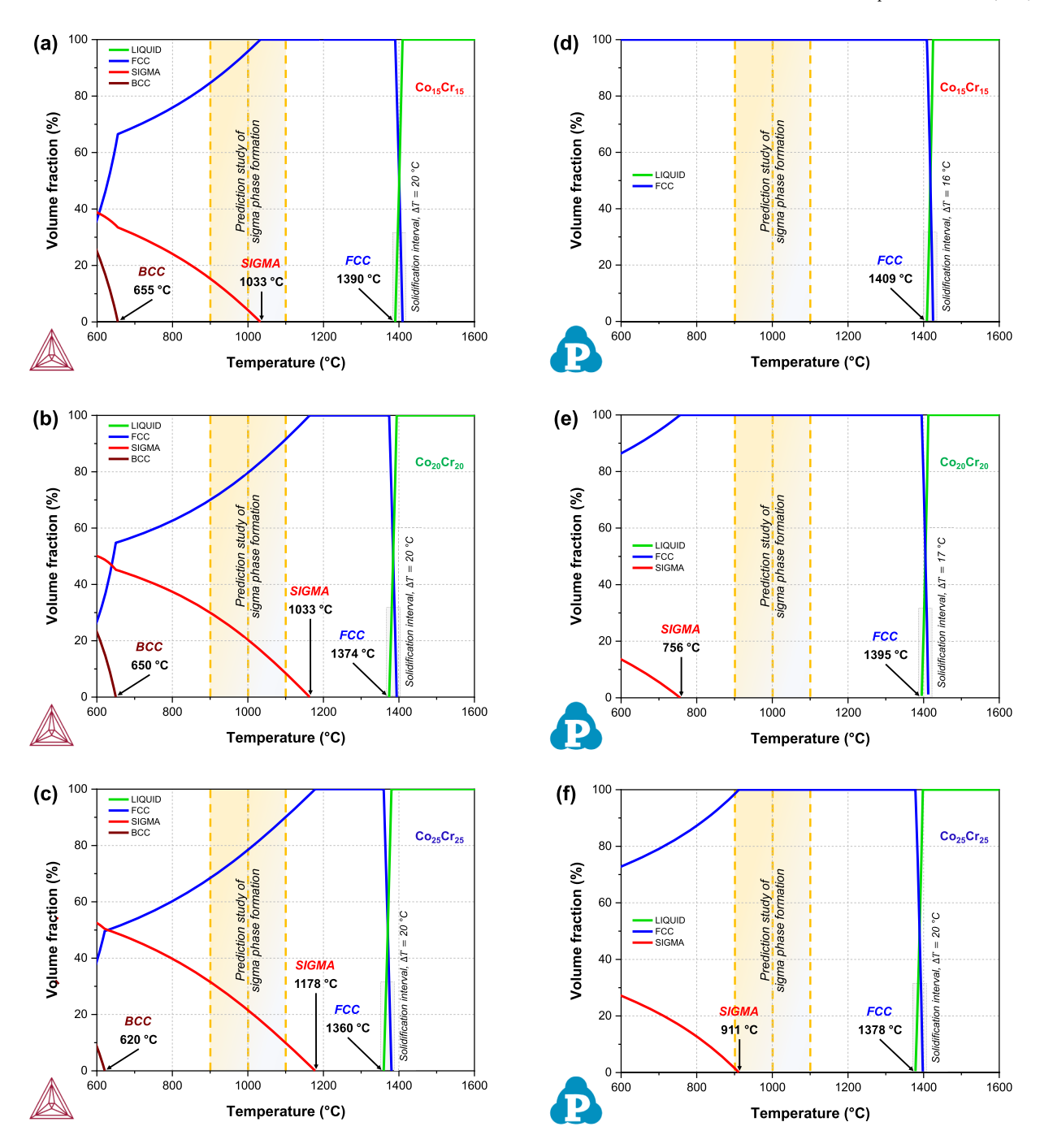


Fig. 1. Equilibrium volume fraction of phases calculated by the CALPHAD method at different temperatures for (a, d) $Co_{15}Cr_{15}$, (b, e) $Co_{20}Cr_{20}$ and (c, f) $Co_{25}Cr_{25}$ alloy. Thermo-Calc® software using TCHEA5 database, and Pandat® software using PanHEA2022 database were used to calculate Fig. 2 (a-c) and Fig. 2 (d-f), respectively. The highlighted regions in golden in the diagrams represent the temperatures chosen (900 °C, 1000 °C, and 1100 °C) to predict sigma phase formation. It should be noted that these thermodynamic calculations were performed under equilibrium conditions. The data were plotted using nominal, rather than actual, alloy compositions. (For interpretation of the references to color in this figure legend, the reader is referred to the Web version of this article.).

(600–900 °C). Fig. 1 (a-f) also shows that when selecting the temperature range between 900 °C and 1100 °C, the phases predictions using TCHEA5 and PanHEA2022 databases completely diverged. Therefore, to assess the accuracy of the CALPHAD method by using two different databases for predicting the formation of the sigma phase, temperatures of 900, 1000, and 1100 °C were selected for thermal aging treatments.

Fig. 2 (a-p) shows the CALPHAD phase equilibria predictions for FeCr $_{50}$ Co $_{50}$ —Ni $_{50}$ Mn $_{50}$ pseudo-ternary phase diagrams at 1200, 1100, 1000, and 900 °C. Decreasing the temperature from 1200 to 900 °C, the FCC phase field shrinks significantly and favors the formation of the

sigma phase, especially for the Cr and Co-rich alloys. However, when comparing the CALPHAD predictions using the TCHEA5 (Fig. 2 (a-h)) and PanHEA2022 (Fig. 2 (i-p)) databases results have revealed a completely different behavior. On the one hand, the calculations using the TCHEA5 database predicted the formation of sigma phase for the Co20Cr20 and Co25Cr25 alloys at 1100 °C and for the three alloys (Co15Cr15, Co20Cr20, and Co25Cr25) at 1000 and 900 °C. On the other hand, the sigma phase formation was only predicted for the Co25Cr25 alloy at 900 °C when the PanHEA2022 database was used, highlighting the importance of database selection. To ensure the viability of the

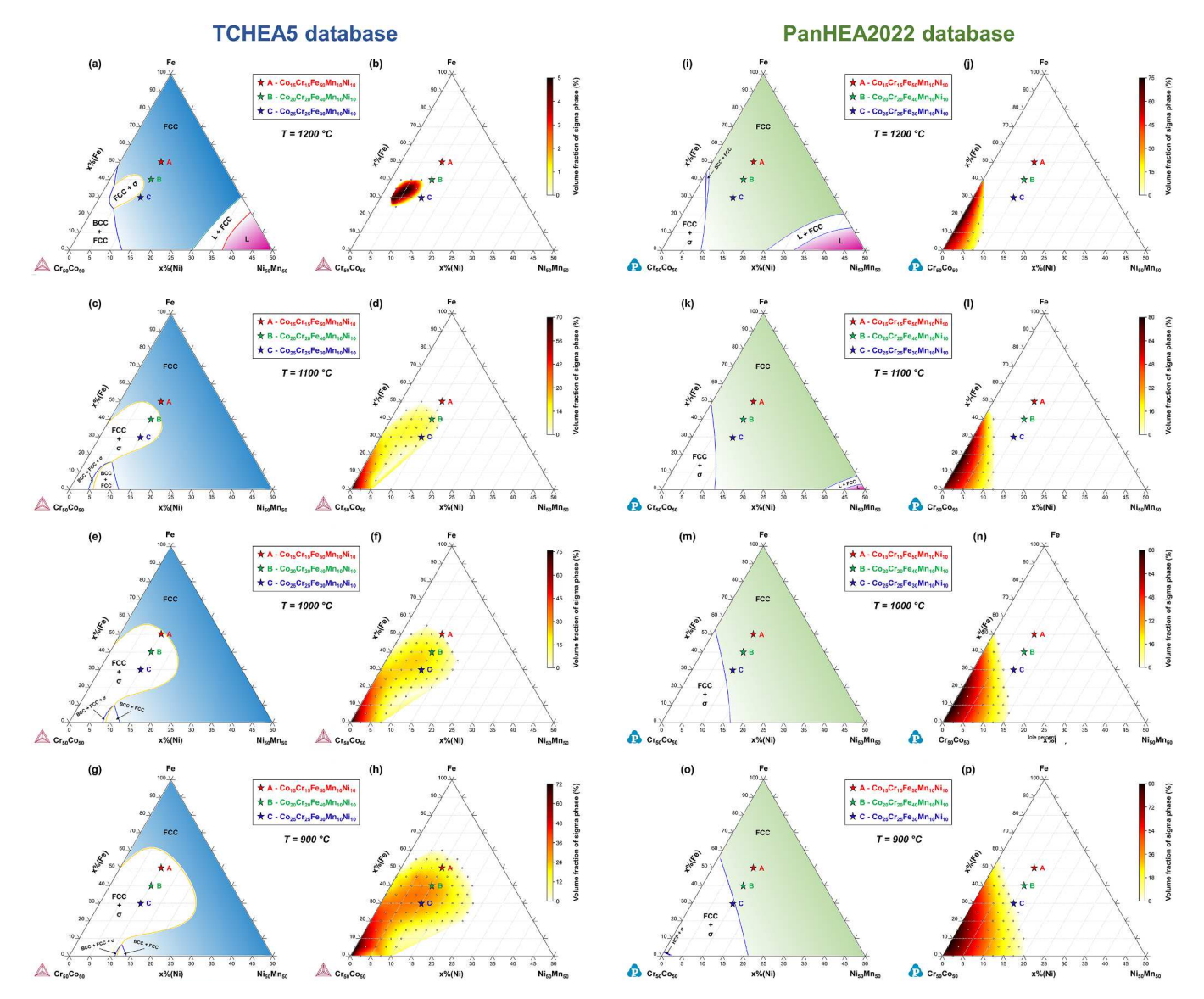


Fig. 2. Pseudo-ternary phase diagram (in at.%) for the Fe-Cr₅₀Co₅₀—Ni₅₀Mn₅₀ system. All single-phase fields are identified. Panels (a, c, e, g) show the 1200 °C, 1100 °C, 1000 °C, and 900 °C isotherms, respectively, and Panels (b, d, f, h) display the calculated volume fraction of sigma phase (%) over the (FCC $+\sigma$) region predicted by Thermo-Calc® software using TCHEA5 database. Panels (i, k, m, o) show the 1200 °C, 1100 °C, 1000 °C, and 900 °C isotherms, respectively, and Panels (j, l, n, p) display the calculated volume fraction of sigma phase (%) over the (FCC $+\sigma$) region predicted by Pandat® software using PanHEA2022 database. The dark gray points in panels ((b, d, f, h), (j, l, n, p)) depict predicted sigma phase fractions by the CALPHAD method. A Python code was developed for calculating additional data points within the range of known data points using bilinear interpolation. The colored stars in panels (a-p) represent the three alloys produced in this study. These thermodynamic calculations were performed under equilibrium conditions. The data were plotted using nominal, rather than actual, alloy compositions. (For interpretation of the references to color in this figure legend, the reader is referred to the Web version of this article.).

CALPHAD method and accuracy of the database used, it is critical to compare predictions to the experimental data.

Previous investigators have studied the effects of alloying elements on the phase stability in the CoCrFeMnNi system, and it is well established that the sigma phase is strongly stabilized by both Cr and Mn, with Cr playing a much more significant role than Mn, or the combination of Cr with Mn [16,17,31–33]. In contrast, Ni, Co, and Fe are strong FCC stabilizers, suppressing the formation of the sigma phase [13, 32,34–36]. To date, similarly detailed studies have not been conducted, when simultaneously varying Co and Cr in equivalent ratios, at the expense of Fe, while keeping Ni and Mn constant, and as a result, the synergistic effects of these elements (Co and Cr) remain unclear. Independent of database used, the CALPHAD calculations indicate a pronounced Cr-driven stabilization of the sigma phase, outweighing the influence of Co on FCC phase stability. A concurrent increase in Co and Cr concentrations in equivalent ratios yields a higher volumetric fraction

of the predicted sigma phase, rendering it progressively thermodynamically favored, irrespective of temperature.

Tsai criteria predictions using two empirical methods, VEC and PSFE, are shown in Fig. 3. To further explore the dimension of the compositional fields, the predictions were expanded to a wide range of compositions, in which pseudo-ternary diagrams for the FeCr $_{50}$ Co $_{50}$ —Ni $_{50}$ Mn $_{50}$ system are presented in Fig. 3 (a, b) for the VEC and PSFE predictions, respectively. Furthermore, to make the Tsai criteria clearer and more intuitive, a graphical representation was generated, as shown in Fig. 3(c). Through the correlation between PSFE and VEC, three distinct zones can be observed: sigma-free, sigma-prone, and uncertain. The Tsai criteria predictions diverged when used the TCHEA5 database, since the Tsai criteria did not predict sigma phase formation for the alloys studied. However, special attention should be paid to the Co20Cr20 and Co25Cr25 alloys, since these alloys present the VEC and PSFE close to the boundary for sigma phase formation. Moreover, it is

D.D.S. Silva et al. Scripta Materialia 252 (2024) 116264

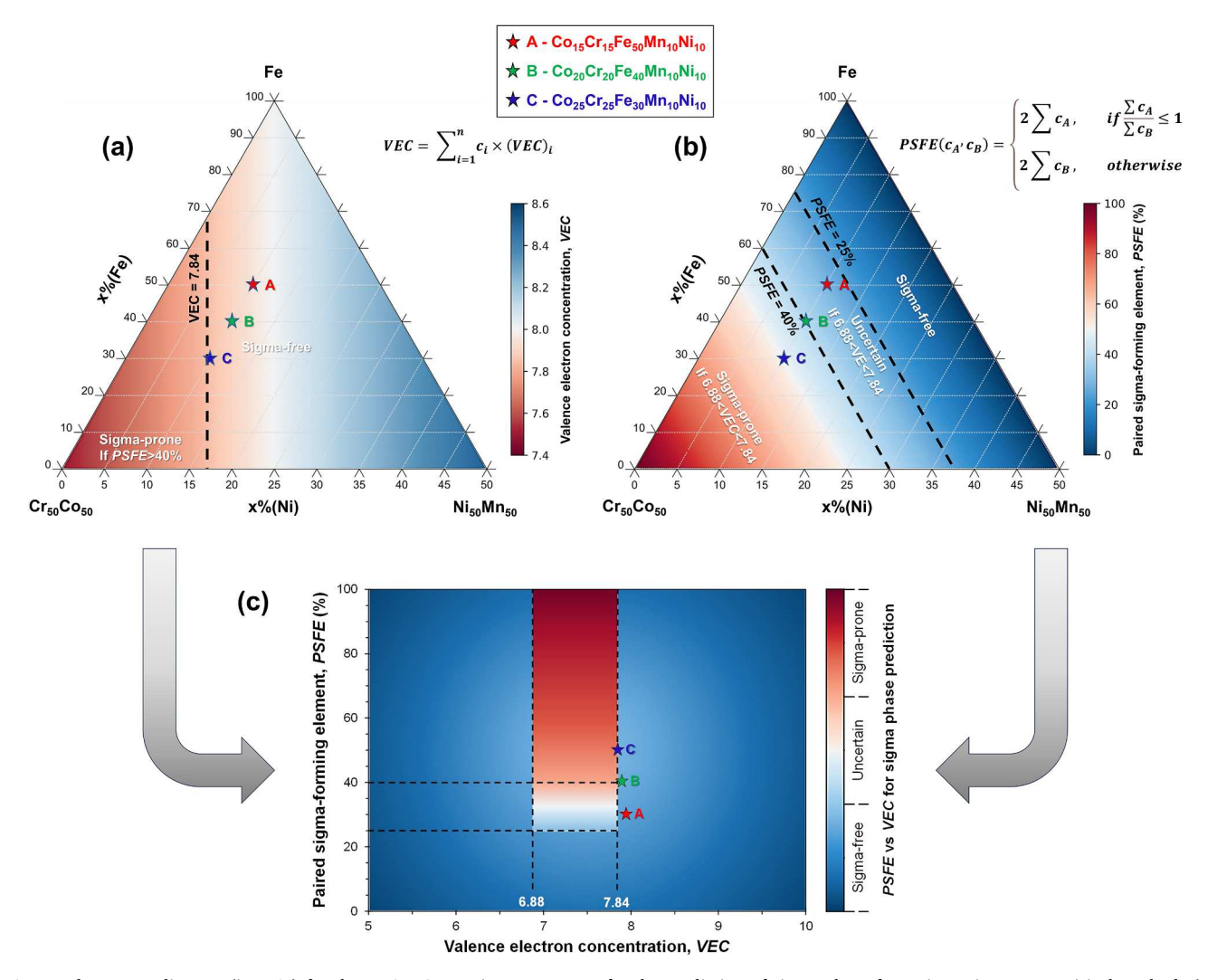


Fig. 3. Pseudo-ternary diagram (in at.%) for the Fe-Cr $_{50}$ Co $_{50}$ —Ni $_{50}$ Mn $_{50}$ system for the prediction of sigma phase formation using two empirical methods (Tsai criteria). (a) Valence electron concentration (VEC) and (b) Paired sigma-forming element (PSFE). It should be noted that different color bars are used for VEC (a) and PSFE (b) diagrams to better represent different ranges. Specifically, the color bar of the VEC diagram ranges from the lowest values (red for weak intensity) to the highest values (blue for strong intensity), while that in the PSFE diagram ranges from the lowest values (blue for weak intensity) to the highest values (red for strong intensity). (c) Correlation between PSFE and VEC for sigma phase prediction by the Tsai criteria indicated by the colored zones. Sigma-free (VEC outside 6.88–7.84 *or* PSFE < 25 % - blue zone); sigma-prone (VEC inside 6.88–7.84 *and* PSFE > 40 % - red zone); and Uncertain (VEC inside 6.88–7.84 *and* PSFE between 25 % and 40 % - light blue/red zone). To further reduce the field of uncertainty, lower and upper PSFE limits were established as 25 % and 40 %, respectively. A Python code was developed to calculate the VEC/PSFE for each composition over the same composition space (pseudo-ternary diagram in at.% for the Fe-Cr $_{50}$ Co $_{50}$ -Ni $_{50}$ Mn $_{50}$ system) with increments of 0.5 at.%. (For interpretation of the references to color in this figure legend, the reader is referred to the Web version of this article.).

important to emphasize that the validation of these empirical methods (VEC/PSFE) demands precise experimental investigations.

The actual compositions deviate only slightly from the designed compositions ($Co_{14.9}Cr_{13.8}Fe_{49.5}Mn_{11.4}Ni_{10.3}Al_{0.1}$, $Co_{19.3}Cr_{18.5}Fe_{39.4}Mn_{11.4}Ni_{10.3}Al_{0.1}$, and $Co_{23.4}Cr_{22.2}Fe_{32.5}Mn_{10.4}Ni_{10.5}$ $Al_{0.1}$, in at. %). Furthermore, the measured total contents of C, S, O, N, and H were below 355, 65, 315, 225, and 35 wt. ppm, respectively, for all alloys, which is relatively low. The presence of these interstitial elements is highly likely due to contamination of the melting equipment and the starting feedstocks used in the fabrication of the alloys.

Representative microstructures of recrystallized and aged samples are presented in Fig. 4. The EBSD inverse pole figure analysis reveals the average grain sizes range from 4.0 to 156.5 μm (Co15Cr15), 3.8 to 75.4 μm (Co20Cr20), and 2.7 to 67.3 μm (Co25Cr25) compared to the recrystallized sample (900 °C for 0.25 h) and the 1100 °C for 20 h condition. It implies these alloys present different grain growth kinetics. Despite 20 h of aging at 900, 1000, and 1100 °C, it was observed that the sigma phase did not form in any of these alloys. Instead, all alloys

consistently retained a single FCC phase. Although Co is not as effective as Ni in suppressing the formation of the sigma phase, it does stabilize the FCC phase, and its effect must be considered.

Although the interstitial elements concentrations in the M/HEAs were at ppm levels, NMIs were observed. To further clarify the microstructure and elemental composition, SEM-BSE/EDS analysis was performed; the results are also shown in Fig. 4. Based on SEM-BSE/EDS qualitative analysis, the NMIs consist of a mixture of oxide, sulfide, and carbide compounds, categorized as follows: Al-rich, (Mn,Al)-rich, and (Mn,Cr)-rich oxides; Mn-rich sulfides; and Cr-rich and Mn-rich carbides. Further details on the identification of the NMIs types through a joint analysis with SEM-BSE/EDS and from the viewpoint of thermodynamics (Gibbs free energies of formation,) can be found in the Supplementary Material. However, a detailed analysis of composition and structure of the NMIs is beyond the scope of this work.

Integration of the obtained 2D diffraction rings into diffraction patterns is detailed in Fig. 5, revealing the dominance of an FCC phase with very low traces of NMIs. The patterns were indexed to the FCC phase and

Scripta Materialia 252 (2024) 116264

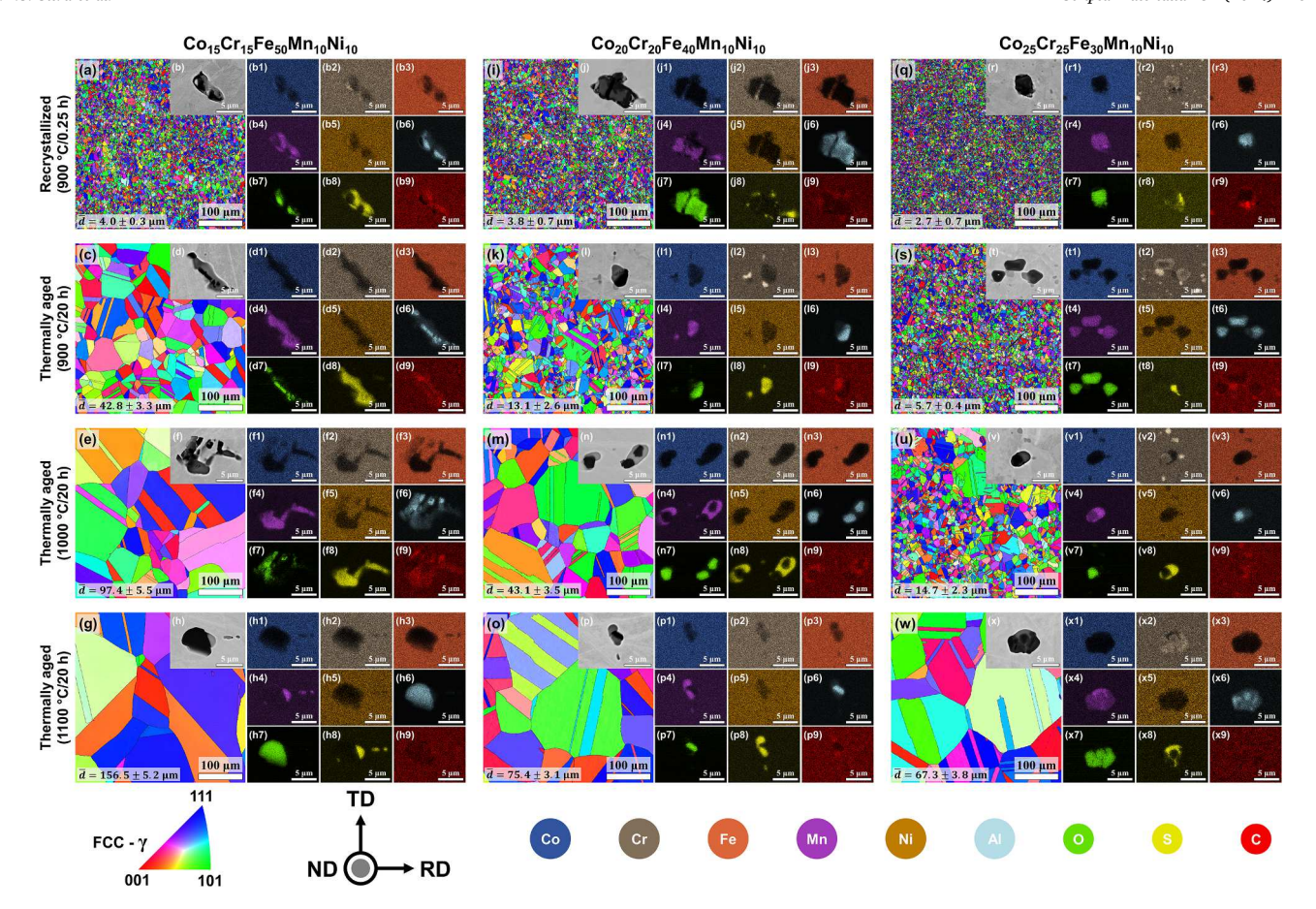


Fig. 4. Representative microstructure of M/HEAs (samples recrystallized and thermally aged). EBSD inverse pole figures (IPFs) of (a, c, e, g) Co15Cr15, (I, k, m, o) Co20Cr20, and (q, s, u, w) Co25Cr25 M/HEAs. SEM-BSE images of the typical non-metallic inclusions (NMIs) found in (b, d, f, h) Co15Cr15, (j, l, n, p) Co20Cr20, and (r, t, v, x) Co25Cr25. (b1-b9), (d1-d9), (f1-f9), (b1-h9), (j1-j9), (l1-l9), (n1-n9), (p1-p9), (r1-r9), (v1-v9), and (x1-x9) correspond to EDS mapping of the NMIs shown in (b, d, f, h) Co15Cr15, (j, l, n, p) Co20Cr20, and (r, t, v, x) Co25Cr25, respectively. The mean grain size (\overline{d}) of each alloy is also indicated in the IPFs. High-angle grain boundaries (HAGBs) with misorientations (θ) \geq 15° are represented by the black lines. Only HAGBs (excluding twin boundaries) were considered to measure the mean grain sizes. Three directions are identified: normal direction (ND), transverse direction (TD), and rolling direction (RD). The color code in the orientation maps represents a specific orientation parallel to the ND (out of the screen) of the alloy sheets according to the key stereographic triangle. (For interpretation of the references to color in this figure legend, the reader is referred to the Web version of this article.).

NMIs, such as Al-rich oxide, (Mn,Cr)-rich oxide, (Mn,Al)-rich oxide, Mnrich sulfide and $M_{23}C_6$ carbide. These findings were consistent with SEM-BSE/EDS examinations. The low-intensity diffraction peaks at specific 2θ positions (dashed line) can be attributed to FCC phase reflections caused by the 2nd harmonic [37–40].

Despite efforts to increase sigma phase formation kinetics by coldrolling the alloys before thermal aging [29], both SEM-BSE/EDS and HE-SXRD analyses suggested the change in driving force and acceleration of sigma phase formation kinetics may not have been sufficient. Schuh et al. [29] suggested the absence of clear experimental evidence of the sigma phase could possibly be attributed to kinetic suppression, rather than thermodynamic stability, implying thermodynamic equilibrium may not have been reached, even after prolonged aging at specific temperatures. However, this possibility seems remote, considering the long time (20 h) the samples were held at a high temperature, 900 °C (and above), which corresponds to 68 % (and above) of the homologous temperature. Additionally, since the samples from this work were previously cold worked, it reinforces the idea that these samples should indeed be sigma-free at the temperatures investigated. Further details on the comparative analysis of sigma phase prediction methods/criteria vs experimental data can be found in the Supplementary Material.

In summary, after presenting and discussing the different aspects of sigma phase prediction methods (CALPHAD and Tsai criteria) and experimental characterization (SEM-BSE/EDS and HE-SXRD analysis),

this work provides valuable guidance for further studies on CoCrFeMnNi M/HEAs that might be susceptible to the formation of the sigma phase. The discussions and critiques presented in this study help to further delineate the compositional fields of M/HEAs with enhanced FCC phase stability, providing guidance for future research in the CoCrFeMnNi system and the avoidance of the deleterious sigma phase.

Data availability

The data supporting the findings in this study are available within the paper. Any further information or clarification is available from the corresponding author upon reasonable request.

CRediT authorship contribution statement

David D.S. Silva: Writing – review & editing, Writing – original draft, Visualization, Validation, Software, Methodology, Investigation, Formal analysis, Data curation, Conceptualization. Gustavo Bertoli: Writing – review & editing, Visualization, Software, Investigation, Formal analysis. Nelson D. Campos Neto: Writing – review & editing, Visualization, Formal analysis. Norbert Schell: Writing – review & editing, Visualization, Formal analysis. Kester D. Clarke: Writing – review & editing, Visualization, Formal analysis. Michael J. Kaufman: Writing – review & editing, Supervision, Funding acquisition, Formal analysis, Conceptualization. Amy J. Clarke: Writing – review & editing,

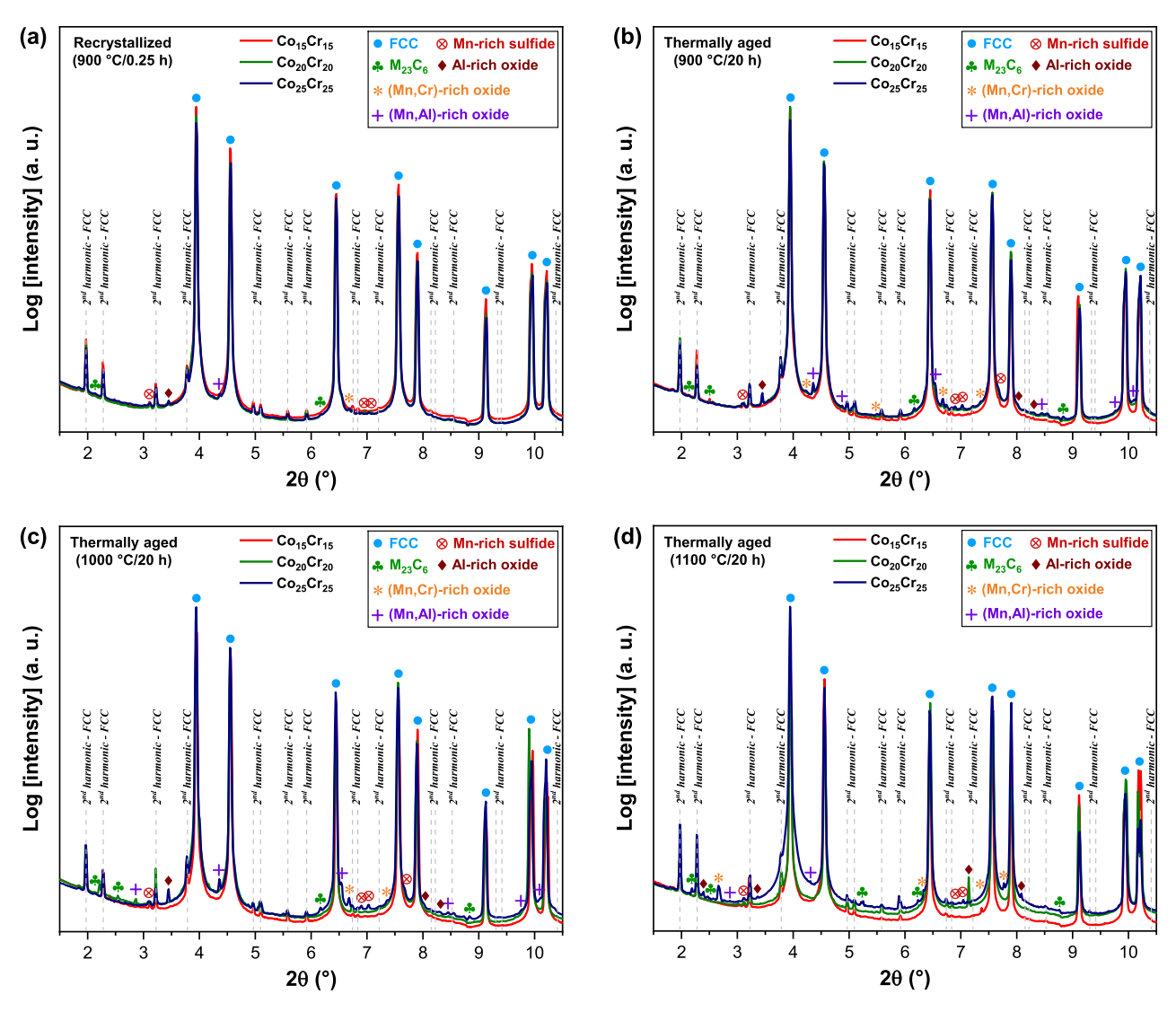


Fig. 5. Representative high-energy synchrotron X-ray diffraction patterns (logarithmic intensity scale) of the M/HEAs. (a) recrystallized at 900 °C for 0.25 h, (b) thermally aged at 900 °C for 20 h, (c) thermally aged at 1000 °C for 20 h, and (d) thermally aged at 1100 °C for 20 h. As shown, peaks of the FCC phase were predominantly observed, along with very weak signals corresponding to non-metallic inclusions (NMIs) identified as oxides, sulfides, and carbides. The unindexed, low-intensity diffraction peaks (dashed line) correspond to FCC phase reflections caused by the 2nd harmonic of the synchrotron X-ray beam. Notably, no indications of the sigma phase were detected. More detailed confirmation of the absence of the sigma phase is available in Fig. 6. The data were plotted by integrating the 2D diffraction patterns along the full azimuthal angle integration. (For color interpretation of the references in this figure legend, please refer to the Web version of this article.).

Supervision, Funding acquisition, Formal analysis, Conceptualization. Francisco G. Coury: Writing – review & editing, Supervision, Funding acquisition, Formal analysis, Conceptualization. Claudemiro Bolfarini: Writing – review & editing, Supervision, Funding acquisition, Formal analysis, Conceptualization.

Declaration of competing interests

The authors declare that they have no known competing financial interests or personal relationships that could have appeared to influence the work reported in this paper.

Acknowledgments

The authors would like to acknowledge the support from the Conselho Nacional de Desenvolvimento Científico e Tecnológico (CNPq/Brazil, grant number 200214/2022–5), Coordenação de Aperfeiçoamento de Pessoal de Nível Superior (CAPES/Brazil, finance code 001),

Fundação de Amparo à Pesquisa do Estado de São Paulo (FAPESP/ Brazil, grant numbers 2021-05408-4, 2022/02770-7 and 2023/ 03385-2), and the Center for Advanced Non-Ferrous Structural Alloys (CANFSA), a National Science Foundation Industry/University Cooperative Research Center (I/UCRC) [Award No. 2137243] at the Colorado School of Mines (CSM) for support during the preparation of this manuscript. The authors also acknowledge the National Science Foundation (DMR-1828454) for the TESCAN S8252G scanning electron microscope. This research used facilities of the Deutsches Elektronen-Synchrotron (DESY), Hamburg, Germany, a member of the Helmholtz Association HGF. Parts of this research were carried out at PETRA III P07B Beamline. Beamtime was allocated for proposal I-20220798. AJC and KDC were supported by the U.S. Department of Energy through the Los Alamos National Laboratory during the preparation of this manuscript. Los Alamos National Laboratory is operated by Triad National Security, LLC, for the National Nuclear Security Administration of U.S. Department of Energy (Contract No. 89233218CNA000001).

Supplementary materials

Supplementary material associated with this article can be found, in the online version, at doi:10.1016/j.scriptamat.2024.116264.

References

- [1] D.B. Miracle, O.N. Senkov, A critical review of high entropy alloys and related concepts, Acta Mater 122 (2017) 448–511, https://doi.org/10.1016/j.
- [2] D. Liu, Q. Yu, S. Kabra, M. Jiang, P. Forna-Kreutzer, R. Zhang, M. Payne, F. Walsh, B. Gludovatz, M. Asta, A.M. Minor, E.P. George, R.O. Ritchie, Exceptional fracture toughness of CrCoNi-based medium- and high-entropy alloys at 20 kelvin, Science (80-.) 378 (2022) 978–983, https://doi.org/10.1126/science.abp8070.
- [3] K. Ming, L. Li, Z. Li, X. Bi, J. Wang, Grain boundary decohesion by nanoclustering Ni and Cr separately in CrMnFeCoNi high-entropy alloys, Sci. Adv. 5 (2019), https://doi.org/10.1126/sciadv.aav0639.
- [4] G. Laplanche, A. Kostka, O.M. Horst, G. Eggeler, E.P. George, Microstructure evolution and critical stress for twinning in the CrMnFeCoNi high-entropy alloy, Acta Mater 118 (2016) 152–163, https://doi.org/10.1016/j.actamat.2016.07.038
- [5] Y. Deng, C.C. Tasan, K.G. Pradeep, H. Springer, A. Kostka, D. Raabe, Design of a twinning-induced plasticity high entropy alloy, Acta Mater 94 (2015) 124–133, https://doi.org/10.1016/j.actamat.2015.04.014.
- [6] M.J. Yao, K.G. Pradeep, C.C. Tasan, D. Raabe, A novel, single phase, non-equiatomic FeMnNiCoCr high-entropy alloy with exceptional phase stability and tensile ductility, Scr. Mater. 72–73 (2014) 5–8, https://doi.org/10.1016/j.scriptamat.2013.09.030.
- [7] Z. Li, K.G. Pradeep, Y. Deng, D. Raabe, C.C. Tasan, Metastable high-entropy dual-phase alloys overcome the strength-ductility trade-off, Nature 534 (2016) 227–230, https://doi.org/10.1038/nature17981.
- [8] F.G. Coury, T. Butler, K. Chaput, A. Saville, J. Copley, J. Foltz, P. Mason, K. Clarke, M. Kaufman, A. Clarke, Phase equilibria, mechanical properties and design of quaternary refractory high entropy alloys, Mater. Des. 155 (2018) 244–256, https://doi.org/10.1016/j.matdes.2018.06.003.
- [9] B.S. Murty, J.-W. Yeh, S. Ranganathan, P.P. Bhattacharjee, High-entropy alloys, 2019
- [10] F. Zhang, C. Zhang, S.L. Chen, J. Zhu, W.S. Cao, U.R. Kattner, An understanding of high entropy alloys from phase diagram calculations, Calphad 45 (2014) 1–10, https://doi.org/10.1016/j.calphad.2013.10.006.
- [11] O.N. Senkov, J.D. Miller, D.B. Miracle, C. Woodward, Accelerated exploration of multi-principal element alloys for structural applications, Calphad 50 (2015) 32–48, https://doi.org/10.1016/j.calphad.2015.04.009.
- [12] G. Bertoli, V.G.L. de Sousa, D. de A. Santana, L.B. Otani, C.S. Kiminami, F.G. Coury, Phase equilibria of VCrMnFeCo high entropy alloys, J. Alloys Compd. 903 (2022) 163950, https://doi.org/10.1016/j.jallcom.2022.163950.
- [13] M.E. Bloomfield, K.A. Christofidou, N.G. Jones, Effect of Co on the phase stability of CrMnFeCoxNi high entropy alloys following long-duration exposures at intermediate temperatures, Intermetallics 114 (2019) 106582, https://doi.org/ 10.1016/j.intermet.2019.106582.
- [14] M.-H. Tsai, J.-H. Li, A.-C. Fan, P.-H. Tsai, Incorrect predictions of simple solid solution high entropy alloys: cause and possible solution, Scr. Mater. 127 (2017) 6–9, https://doi.org/10.1016/j.scriptamat.2016.08.024.
- [15] A. Kumar, M. Abu Shaz, N.K. Mukhopadhyay, T.P. Yadav, Phase transformation of AB5 to AB2 type phase on substitution of Mn with Zr in TiVCoNi (ZrxMn2-x) (x = 0, 0.3, 0.6, 1.0) high entropy alloys, Mater. Chem. Phys. 318 (2024) 129291, https://doi.org/10.1016/j.matchemphys.2024.129291.
- [16] G. Laplanche, S. Berglund, C. Reinhart, A. Kostka, F. Fox, E.P. George, Phase stability and kinetics of σ-phase precipitation in CrMnFeCoNi high-entropy alloys, Acta Mater 161 (2018) 338–351, https://doi.org/10.1016/j.actamat.2018.09.040.
- [17] G. Laplanche, Growth kinetics of σ-phase precipitates and underlying diffusion processes in CrMnFeCoNi high-entropy alloys, Acta Mater 199 (2020) 193–208, https://doi.org/10.1016/j.actamat.2020.08.023.
- [18] A.J. Zaddach, R.O. Scattergood, C.C. Koch, Tensile properties of low-stacking fault energy high-entropy alloys, Mater. Sci. Eng. A. 636 (2015) 373–378, https://doi. org/10.1016/j.msea.2015.03.109.
- [19] K. Ming, X. Bi, J. Wang, Microstructures and deformation mechanisms of Cr26Mn20Fe20Co20Ni14 alloys, Mater. Charact. 134 (2017) 194–201, https://doi. org/10.1016/j.matchar.2017.10.022.
- [20] D.D.S. Silva, T.A. Simões, D.A. Macedo, A.H.S. Bueno, S.M. Torres, R.M. Gomes, Microstructural influence of sigma phase on pitting corrosion behavior of duplex

- stainless steel/NaCl electrolyte couple, Mater. Chem. Phys. 259 (2021) 124056, https://doi.org/10.1016/j.matchemphys.2020.124056.
- [21] D.D.S. Silva, J.M.B. Sobrinho, C.R. Souto, R.M. Gomes, Application of electromechanical impedance technique in the monitoring of sigma phase embrittlement in duplex stainless steel, Mater. Sci. Eng. A. 788 (2020) 139457, https://doi.org/10.1016/j.msea.2020.139457.
- [22] D.D.S. Silva, R.A. Raimundo, R.A. Torquato, G.L. Faria, M.A. Morales, T.A. Simões, R.M. Gomes, Low-field magnetic analysis for sigma phase embrittlement monitoring in thermally aged 22Cr duplex stainless steel, J. Magn. Magn. Mater. 513 (2020) 167072, https://doi.org/10.1016/j.jmmm.2020.167072.
- [23] E.P. George, D. Raabe, R.O. Ritchie, High-entropy alloys, Nat. Rev. Mater. 4 (2019) 515–534, https://doi.org/10.1038/s41578-019-0121-4.
- [24] M.H. Tsai, K.Y. Tsai, C.W. Tsai, C. Lee, C.C. Juan, J.W. Yeh, Criterion for sigma phase formation in Cr- and V-containing high-entropy alloys, Mater. Res. Lett. 1 (2013) 207–212, https://doi.org/10.1080/21663831.2013.831382.
- [25] M.H. Tsai, K.C. Chang, J.H. Li, R.C. Tsai, A.H. Cheng, A second criterion for sigma phase formation in high-entropy alloys, Mater. Res. Lett. 4 (2016) 90–95, https:// doi.org/10.1080/21663831.2015.1121168.
- [26] A. Jacob, E. Povoden-Karadeniz, E. Kozeschnik, Revised thermodynamic description of the Fe-Cr system based on an improved sublattice model of the σ phase, Calphad 60 (2018) 16–28, https://doi.org/10.1016/j.calphad.2017.10.002.
- [27] J.-M. Joubert, Crystal chemistry and Calphad modeling of the σ phase, Prog. Mater. Sci. 53 (2008) 528–583, https://doi.org/10.1016/j.pmatsci.2007.04.001.
- [28] ASM Handbook, Alloy Phase Diagrams, 2004.
- [29] B. Schuh, F. Mendez-Martin, B. Völker, E.P. George, H. Clemens, R. Pippan, A. Hohenwarter, Mechanical properties, microstructure and thermal stability of a nanocrystalline CoCrFeMnNi high-entropy alloy after severe plastic deformation, Acta Mater 96 (2015) 258–268, https://doi.org/10.1016/j.actamat.2015.06.025.
- [30] N. Schell, R.V. Martins, F. Beckmann, H.U. Ruhnau, R. Kiehn, A. Schreyer, The high energy materials science beamline at PETRA III, Mater. Sci. Forum. 571–572 (2008) 261–266, https://doi.org/10.4028/www.scientific.net/MSF.571-572.261.
- [31] M. Tian, C. Wu, Y. Liu, H. Peng, J. Wang, X. Su, Phase stability and microhardness of CoCrFeMnxNi2-x high entropy alloys, J. Alloys Compd. 811 (2019) 152025, https://doi.org/10.1016/j.jallcom.2019.152025.
- [32] C. Zhang, J. Zhu, W.S. Cao, S.L. Chen, S.M. Liang, F. Zhang, Development of phase-based databases via CALPHAD method for the design of high-entropy alloys, J. Phase Equilibria Diffus. 43 (2022) 678–690, https://doi.org/10.1007/s11669-022-00970-9
- [33] K.A. Christofidou, E.J. Pickering, P. Orsatti, P.M. Mignanelli, T.J.A. Slater, H. J. Stone, N.G. Jones, On the influence of Mn on the phase stability of the CrMnxFeCoNi high entropy alloys, Intermetallics 92 (2018) 84–92, https://doi.org/10.1016/j.intermet.2017.09.011.
- [34] K.A. Christofidou, T.P. McAuliffe, P.M. Mignanelli, H.J. Stone, N.G. Jones, On the prediction and the formation of the sigma phase in CrMnCoFeNix high entropy alloys, J. Alloys Compd. 770 (2019) 285–293, https://doi.org/10.1016/j. iallcom.2018.08.032.
- [35] M.E. Bloomfield, K.A. Christofidou, F. Monni, Q. Yang, M. Hang, N.G. Jones, The influence of Fe variations on the phase stability of CrMnFexCoNi alloys following long-duration exposures at intermediate temperatures, Intermetallics 131 (2021) 107108, https://doi.org/10.1016/j.intermet.2021.107108.
- [36] Z.G. Zhu, K.H. Ma, X. Yang, C.H. Shek, Annealing effect on the phase stability and mechanical properties of (FeNiCrMn)(100–)Co high entropy alloys, J. Alloys Compd. 605 (2017) 2945–2950. https://doi.org/10.1016/j.iallcom.2016.11.376
- Compd. 695 (2017) 2945–2950, https://doi.org/10.1016/j.jallcom.2016.11.376.
 [37] P. Erdely, P. Staron, E. Maawad, N. Schell, J. Klose, S. Mayer, H. Clemens, Effect of hot rolling and primary annealing on the microstructure and texture of a β-stabilised γ-TiAl based alloy, Acta Mater 126 (2017) 145–153, https://doi.org/10.1016/j.actamat.2016.12.056.
- [38] D. Wimler, J. Lindemann, C. Gammer, P. Spoerk-Erdely, A. Stark, H. Clemens, S. Mayer, Novel intermetallic-reinforced near-α Ti alloys manufactured by spark plasma sintering, Mater. Sci. Eng. A. 792 (2020) 139798, https://doi.org/10.1016/ i.msea.2020.139798.
- [39] S.C. Bodner, M. Meindlhumer, T. Ziegelwanger, H. Winklmayr, T. Hatzenbichler, C. Schindelbacher, B. Sartory, M. Krobath, W. Ecker, N. Schell, J. Keckes, Correlative cross-sectional characterization of nitrided, carburized and shotpeened steels: synchrotron micro-X-ray diffraction analysis of stress, microstructure and phase gradients, J. Mater. Res. Technol. 11 (2021) 1396–1410, https://doi.org/10.1016/j.jmrt.2021.01.099.
- [40] M. Truschner, A. Janda, S.C. Bodner, A. Keplinger, G. Mori, Effect of cold deformation on the stress corrosion cracking resistance of a high-strength stainless steel, J. Mater. Sci. 57 (2022) 20447–20461, https://doi.org/10.1007/s10853-022-07866-6.